Chapter 3

HA nucleation and crystal growth

The current chapter presents the phase evaluation of HA nanocrystals along with profile fitting of XRD peaks using FullProf software to reveal the variation in lattice parameter as per morphology of HA nanocrystals. The morphological analyses of HA nanocrystals are also discussed. The closer analyses using TEM have also been carried out to observe the porous nature and crystal growth direction of HA nanocrystals. Additionally, this chapter also explores the possible molecular mechanism, controlling the growth of different morphological HA nanocrystals.

3.1. XRD analyses

Fig. 3.1 depicts the XRD patterns of all the samples, developed under different pH, HT time, and different concentrations of PVA. All the diffraction peaks correspond to the pure hexagonal phase of HA nanocrystals, aligning well with standard data (JCPDS #09-0432). No additional peaks related to other phases were observed for these samples. From Fig. 3.1 A, it is clearly visible that on altering the pH of precursor solution from pH 5 to 9.5, the intensity of peaks continuously increases gradually and reaches up to the maximum, which reveals that higher pH strongly promotes crystallinity in HA due to increased OH^- ions [1, 2]. HA nanocrystals synthesized at a pH of 9.5 achieved ultra-high crystallinity (97 %), which is 9 % higher than the crystallinity of HA nanocrystals, synthesized at a pH of 5 (89 %). On further increasing the pH (> 9.5), there was no noteworthy change in crystallinity.

The effect of HT time as well as concentrations of PVA on the crystallinity of HA nanocrystals, was also investigated (Fig. 3.1 B). The intensities of HA peaks become higher and sharper on varying the HT period from 6 to 12 h, which indicates that the longer HT time favours the formation of ultra-high crystalline HA [Fig. 3.1 B (i and ii)]. In other words, 6 h is not sufficient for proper crystallization of HA from an amorphous state [3]. Nearly 86 % of crystallinity was

calculated for HA nanocrystals, synthesized at the HT period of 6 h. A slight reduction in the intensity of peaks was also observed on increasing the concentration of PVA from 2.13 – 4.17 wt %, which means that PVA at 4.17 wt % hinders the crystallization of HA [Fig. 3.1 B (ii, iii and iv)]. As a result, the crystallinity of HA nanocrystals was reduced from 97 to 93 %. However, on further varying the concentration of PVA from 4.17 – 6.13 wt %, no significant change in crystallinity was found.

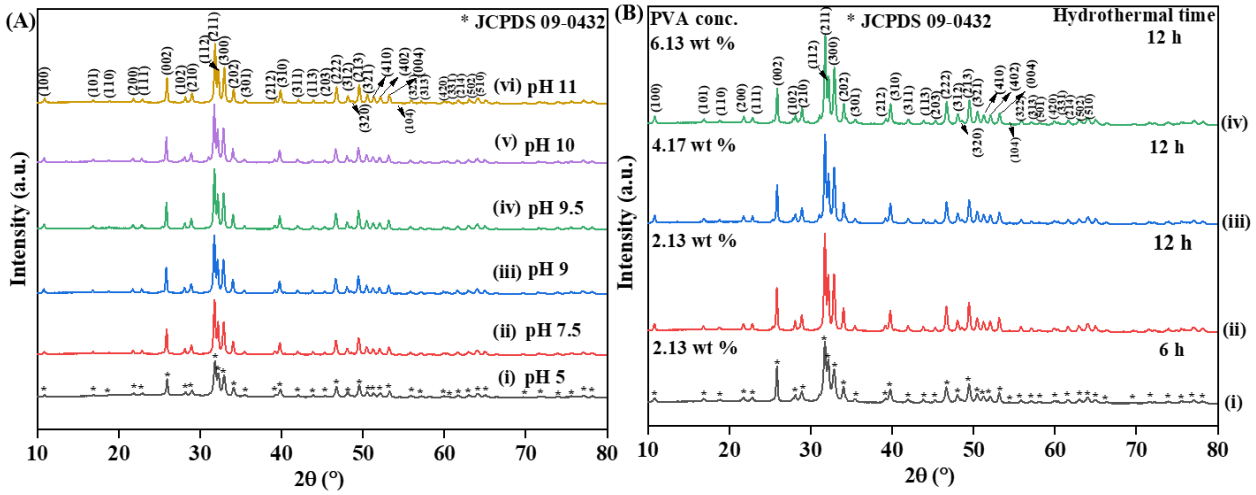

Figure 3.1. XRD profile of HA nanocrystals, synthesized under different pH, HT time, and PVA concentrations. *(A) Characteristic peaks at different pH: (i) pH 5, (ii) pH 7.5, (iii) pH 9, (iv) pH 9.5, (v) pH 10, (vi) pH 11 at constant HT temperature and time of 200ºC and 12 h, respectively, for PVA concentration of 2.13 wt %. (B) Characteristic peaks at different HT time: (i) 6 h and (ii) 12 h at constant pH of 9.5, PVA concentration of 2.13 wt %, HT temperature of 200ºC, and under different PVA concentrations: (ii) 2.13 wt %, (iii) 4.17 wt % and (iv) 6.13 wt % at constant pH of 9.5, HT temperature and time of 200ºC and 12 h, respectively.*

The profile fitting of XRD data of developed HA nanorods (HA5), nanoplates (HA9.5), and thin nanoplates (HA-6h) was performed using FullProf software (Fig. 3.2). The patterns were well refined in hexagonal structure (space group of $P6_3/m$) with goodness of fit of 3.0 and 2.1 and 3.5, respectively. The refined cell parameters were, a = 9.4295 Å, c = 6.8821 Å for HA

nanorods, a = 9.4256 Å, c = 6.8842 Å for HA nanoplates, and a = 9.4282 Å and c = 6.8857 Å for HA thin nanoplates. It is clear that HA nanorods have larger a and smaller c values than those of HA nanoplates and thin nanoplates. The lattice parameter ‘a’ is related to the side growth of HA, which leads to plate shape formation and the lattice parameter ‘c’ is related to the end growth of HA, which leads to the formation of nanorods. It is reported that lattice parameters expand with the decrease in the size of nanocrystals [4, 5]. This is also true for the anisotropic growth of nanocrystals, i.e., the change in shape results in a sudden transition in the lattice parameters, specific to a particular crystal face [6]. As an example, Zhu et al.[7] found that the lattice parameter ‘c’ reduced from 5.263 – 5.230 Å on increasing the length of ZnO nanorods from 10 – 30 nm. In the present study, because of the restriction of crystal growth along the c-axis, HA nanoplates and thin nanoplates have larger lattice parameter ‘c’ as compared to HA nanorods, and due to the restriction of crystal growth along the a-axis, HA nanorods have larger lattice parameter ‘a’, as compared to that of HA nanoplates and thin nanoplates. This variation in lattice parameters, as per morphology, is in good agreement with previously reported data for HA nanorods (a = 9.4330 Å, c = 6.8765 Å) and HA nanoplates (a = 9.4253 Å, c = 6.8877 Å) [8, 9].

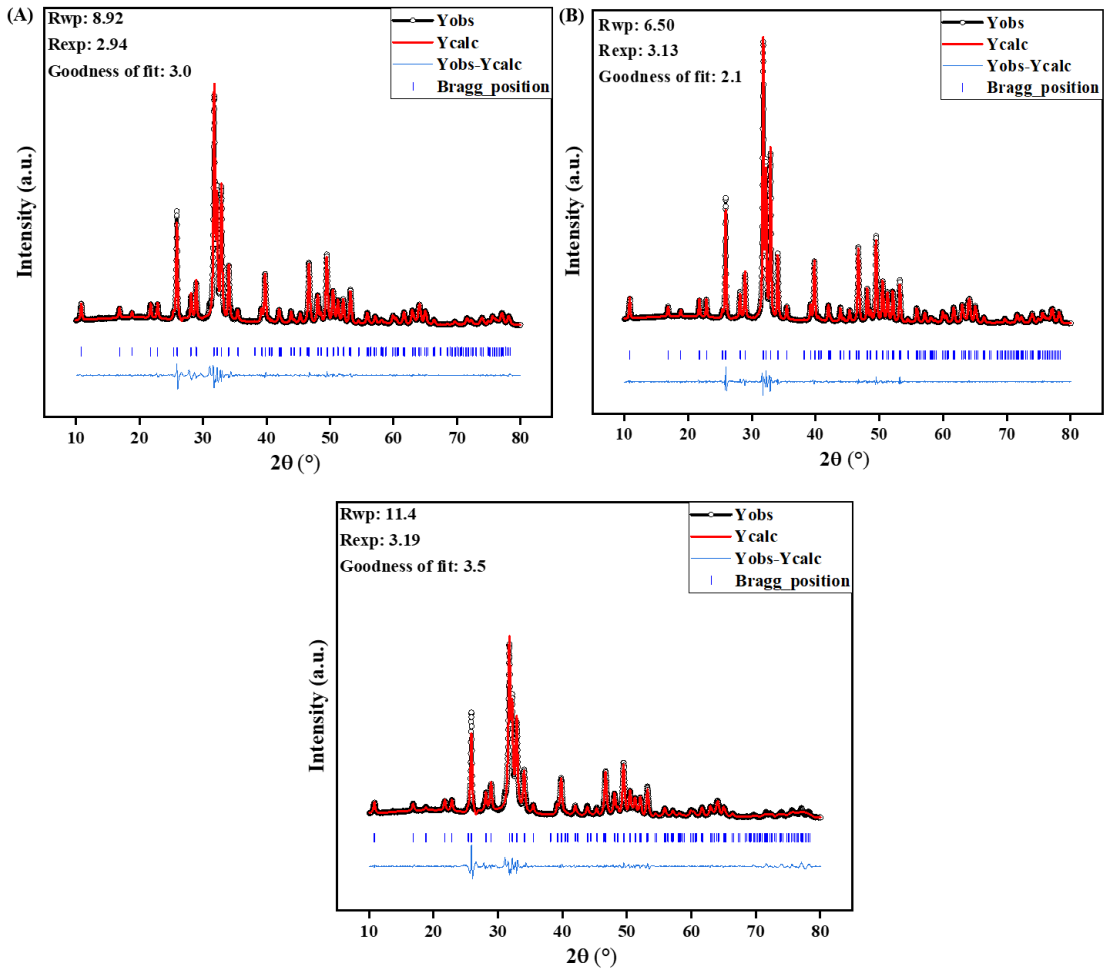

Figure 3.2. *X-ray profile fitting for HA nanorods, nanoplates, and thin nanoplates using FullProf software.*

3.2. FTIR analyses

The functional groups of the developed samples were also analyzed using the FTIR technique to further confirm the phase purity of synthesized samples. The FTIR spectra of all nanocrystals, synthesized at different pH, HT time, and different PVA concentrations, are shown in Fig. 3.3. The characteristic bands at 1099, 1033 and 600, 568 cm^{-1} correspond to asymmetric stretching and bending vibrations of PO_4^{3-} tetrahedra, respectively. Another band, related to PO_4^{3-} at 962 and 473 cm^{-1}, can be assigned to symmetric stretching and bending modes of P–O and O–P–O bonds, respectively [10-12]. The absorption bands at 3574 cm^{-1} and 635 cm^{-1} also appeared due to the stretch and libration modes of OH^- ions in the HA lattice, respectively. The peaks at 3436 cm^{-1} and 1635 cm^{-1} were caused by bending vibration of O –

H in absorbed H_2O [13]. The presence of CO_3^{2-} in HA was also confirmed by the peaks, observed at 1456, 1411, 1544 and 875 cm^{-1} [14]. Such CO_3^{2-} formed when atmospheric CO_2 dissolved in a precursor solution of HA during the fabrication stage, according to the following reaction [15]:

$$CO_{2\,(g)} + 2OH^-_{(aq)} \rightarrow CO_3^{2-}{}_{(aq)} + H_2O_{(l)} \qquad (1)$$

Importantly, this CO_3^{2-} group, which was either substituted by OH^- or PO_4^{3-} groups, is called A-type carbonate (1544 and 875 cm^{-1}) and B-type carbonate (1456 and 1411 cm^{-1}), respectively [16]. From Fig. 3.3 A (i), it is clearly visible that at acidic condition (pH 5), no peak, corresponding to CO_3^{2-} was observed. However, on increasing the pH above 5, A-type and B-type CO_3^{2-} bands started to appear [Fig. 3.3 A (ii)] and continuously increases up to pH 11. As the atmospheric CO_2 dissolves more readily in alkaline conditions, owing to an increase in the availability of OH^- ions. The increase in B-type CO_3^{2-} bands (with rising pH) made the PO_4^{3-} peaks (1095 and 1033 cm^{-1}) gradually broader due to CO_3^{2-} substitution, which is supported by the previous studies [17, 18]. However, no change in the sharpness of OH^- bands was observed, which may be due to the low visibility of A-type carbonate bands. From Fig. 3.3 B (i), it is clearly observed that at lower HT time (6 h), no CO_3^{2-} bands appeared. It means that atmospheric CO_2 is mainly incorporated in solution during HT treatment, as can be seen in HA, synthesized under 12 h of HT period, where sharp CO_3^{2-} bands appeared [Fig. 3.3 B (ii)]. Fig. 3.3 B (ii, iii and iv) shows that on increasing the concentration of PVA from 2.13 to 6.13 wt %, the sharpness of CO_3^{2-} bands decreased and almost disappeared. Consequently, the broad PO_4^{3-} peaks became sharper again. This clearly indicates that a higher concentration of PVA prevents the atmospheric CO_2 to dissolve in the solution. This might be due to the presence of a larger number of PVA molecules to interact with OH^- ions present in the solution, which reduces the free OH^-. As a result, fewer OH^- are available to interact with CO_2 for CO_3^{2-} formation.

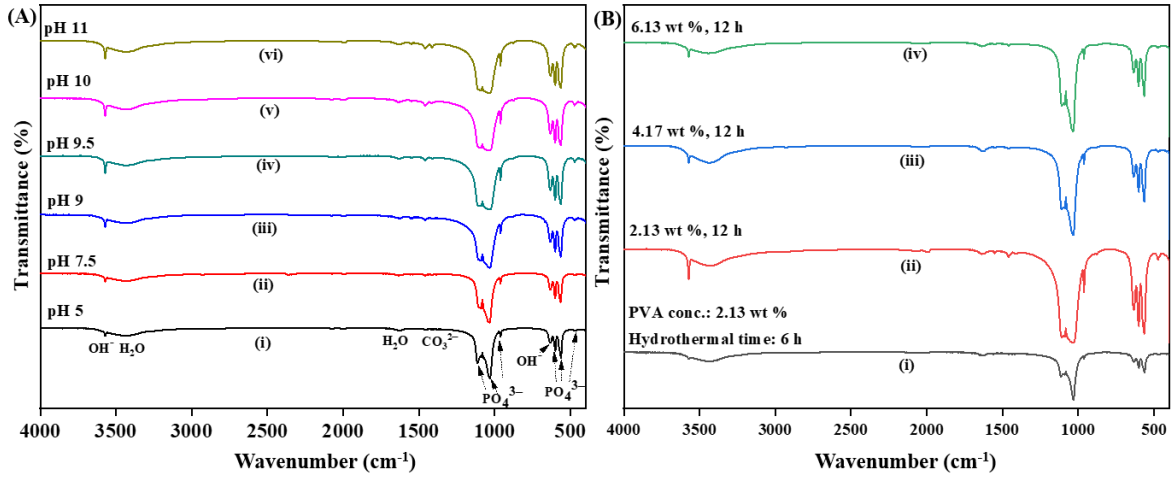

Figure 3.3. FTIR spectra of HA nanocrystals, synthesized at various pH, different HT time and PVA concentrations. *(A) Spectra at various pH: (i) pH 5, (ii) pH 7.5, (iii) pH 9, (iv) pH 9.5, (v) pH 10, and (vi) 11, at constant HT temperature and time of 200ºC and 12 h, respectively, for PVA concentration of 2.13 wt %. (B) Spectra for HT times: (i) 6 h and (ii) 12 h at constant pH of 9.5, PVA concentration of 2.13 wt %, HT temperature of 200ºC, and under various PVA concentrations: (ii) 2.13 wt %, (iii) 4.17 wt % and (ii) 6.13 wt % at constant pH of 9.5, HT temperature and time of 200ºC and 12 h, respectively.*

The crystallinity of HA nanocrystals can also be investigated using FTIR spectra as per the intensity of peaks. A similar variation in the crystallinity profile of HA under different pH, HT time and PVA concentrations was observed, which is in good agreement with XRD results.

3.3. Raman spectroscopic analyses

Raman spectroscopy was performed to investigate the phase purity of developed HA nanorods (HA5), nanoplates (HA9.5), and thin nanoplates (HA-6h) samples by analyzing the chemical species, present as building units in nHA materials. Fig. 3.4 depicts the Raman spectra of prepared samples, showing strong characteristic vibrational bands at 958 cm^{-1}, which corresponds to the ν_1 symmetric stretching mode of P–O within the tetragonal PO_4^{3-} group of HA crystal lattice [19]. Other peaks, appeared at 435, 587 cm^{-1} are assigned to ν_2 and ν_4 symmetric bending mode (P–O–P) of PO_4^{3-} group [20]. The peak at 1047 cm^{-1} appeared from

asymmetric stretching (ν_3) of P−O, which reveals the presence of disordered phosphate lattice within HA nanocrystals [21]. Furthermore, the presence of OH^- ions in the HA lattice is also detected by the vibrational peak at 3570 cm^{-1}, related to the stretching vibration of O – H [21]. No other vibrational bands were observed in all the developed samples, which confirms the formation of the single and pure phases of HA nanocrystals.

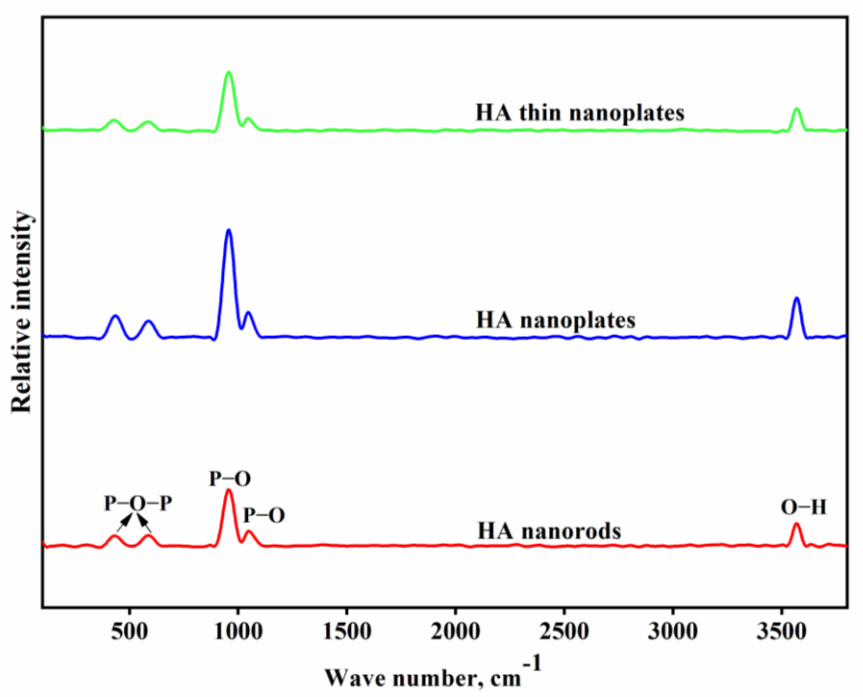

Figure. 3.4. *Raman spectroscopic analysis of HA nanorods (a) and nanoplates (b) prepared at pH 5 and 9.5, respectively, under the constant HT temperature of 200ºC, time of 12 h, and PVA concentration of 2.13 wt %, and HA thin nanoplates (c) prepared HT time of 6 h under constant hydrothermal temperature of 200ºC, pH of 9.5, and PVA concentration of 2.13 wt %.*

3.4. Nanomorphological analyses: crystal growth

The formation of HA nanocrystals proceeded in two steps: (i) nucleation and (ii) crystal growth. Initially, Ca^{2+} ions from calcium nitrate interacted with hydroxyl groups of PVA molecules, resulting in the formation of PVA-Ca complex [22]. However, the subsequent addition of phosphate solution led to the breaking of PVA-Ca complexes due to their weak bonding [22, 23]. The released Ca^{2+} ions interacted with PO_4^{3-} ions, leading to instant HA nucleation due to

supersaturation conditions. After nucleation, the released PVA molecules from PVA-Ca complexes return back to the solution. (pH 5; acidic condition). Fig. 3.5 schematically represents the mechanism of HA nucleation.

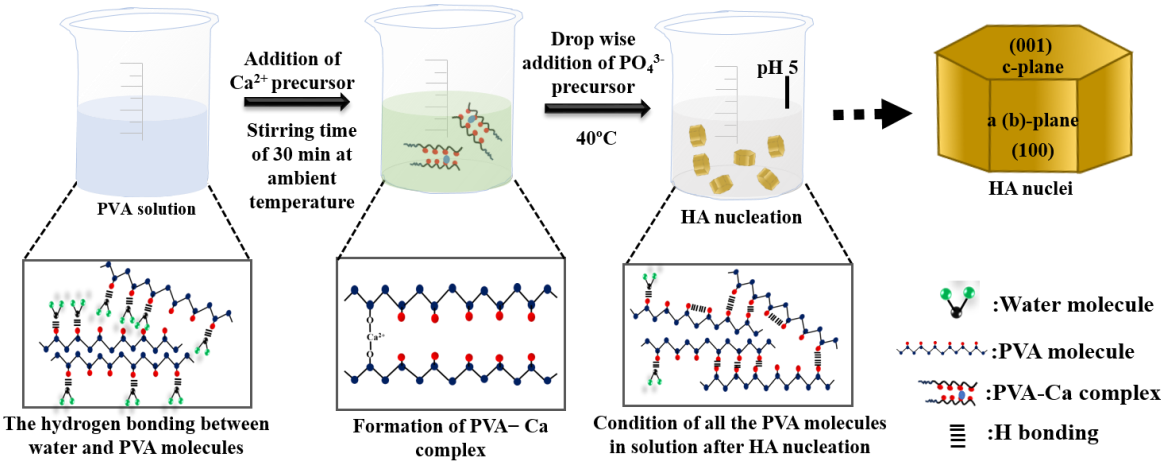

Figure 3.5. *Schematic diagram, demonstrating the possible mechanism behind the nucleation of HA nanocrystals.*

At pH 5, PVA molecules were free to interact with themselves, neighbouring PVA and water molecules through hydrogen bonding [24]. Apparently, no PVA molecule was available to adsorb on the relatively high surface energy (001) facet of HA nuclei to reduce their surface energy. Consequently, it could not restrict the crystal growth of HA nuclei along their thermodynamically favourable [001] direction (c-axis) [25]. Thus, a clear and sharp rod morphology with a length of ~ 70 – 500 nm and a diameter of ~ 22 – 62 nm was formed [Fig. 3.6 (a)]. The gradual addition of NaOH disturbed intra and inter-molecular hydrogen bonding among PVA molecules and between PVA and water molecules as per the following reaction [26-28],

$$R - OH + Na^{+}OH^{-} \rightarrow R - O^{-}\,Na^{+} + H_2O \qquad (2)$$

Therefore, at pH 7.5, few PVA molecules became available to restrict the crystal growth of HA in the c-axis direction. Consequently, most of HA nanocrystals were formed in indefinite shape at pH 7.5. However, a few plate-like HA nanostructures were also observed [Fig. 3.6

(b)]. It may be due to the fact that few OH^- ions also become available to adsorb on (100) facet (side face) of HA nuclei, which makes these faces active for HA crystal growth along [100] direction (a-axis) [29-31]. At pH 9, more PVA molecules restricted the HA crystal growth in [001] direction, and a larger number of OH^- ions adsorbed on (100) facet of HA nuclei to promote crystal growth toward a-axis direction. In this condition, HA nanorods, formed at pH 5, transformed into slightly irregular-shaped 2-D HA nanoplates with a length ranging from ~ 65 – 300 nm and thickness from ~ 21 – 45 nm. [Fig. 3.6 (c)]. Increasing pH to 9.5 further refined plates to regular shape (rectangle as well as hexagonal) with length, diameter and thickness of 200 – 500, 60 – 250, and 7 – 66 nm, respectively, due to the optimal number of OH^- ions which can adsorb uniformly on side faces of HA nuclei [Fig. 3.6 (d)]. Moreover, the thickness of few HA nanoplates was also reduced, owing to the adsorption of more PVA molecules on (001) facet of HA nuclei. Apparently, the broadness in thickness distribution of these HA nanoplates increased as compared to HA nanoplates, prepared at pH 9. The increase in the pH from 9.5 to 10 further increases the size of HA nanoplates, owing to the adsorption of more OH^- ions on the side faces of HA nuclei [Fig. 3.6 (e)]. In this stage, the uniformity in the shape of HA nanoplates again began to destroy. At pH 11, excessive OH^- ions completely disrupted the uniformity, resulting in irregular HA nanoplates and ungrown NPs. [Fig. 3.6 (f)].

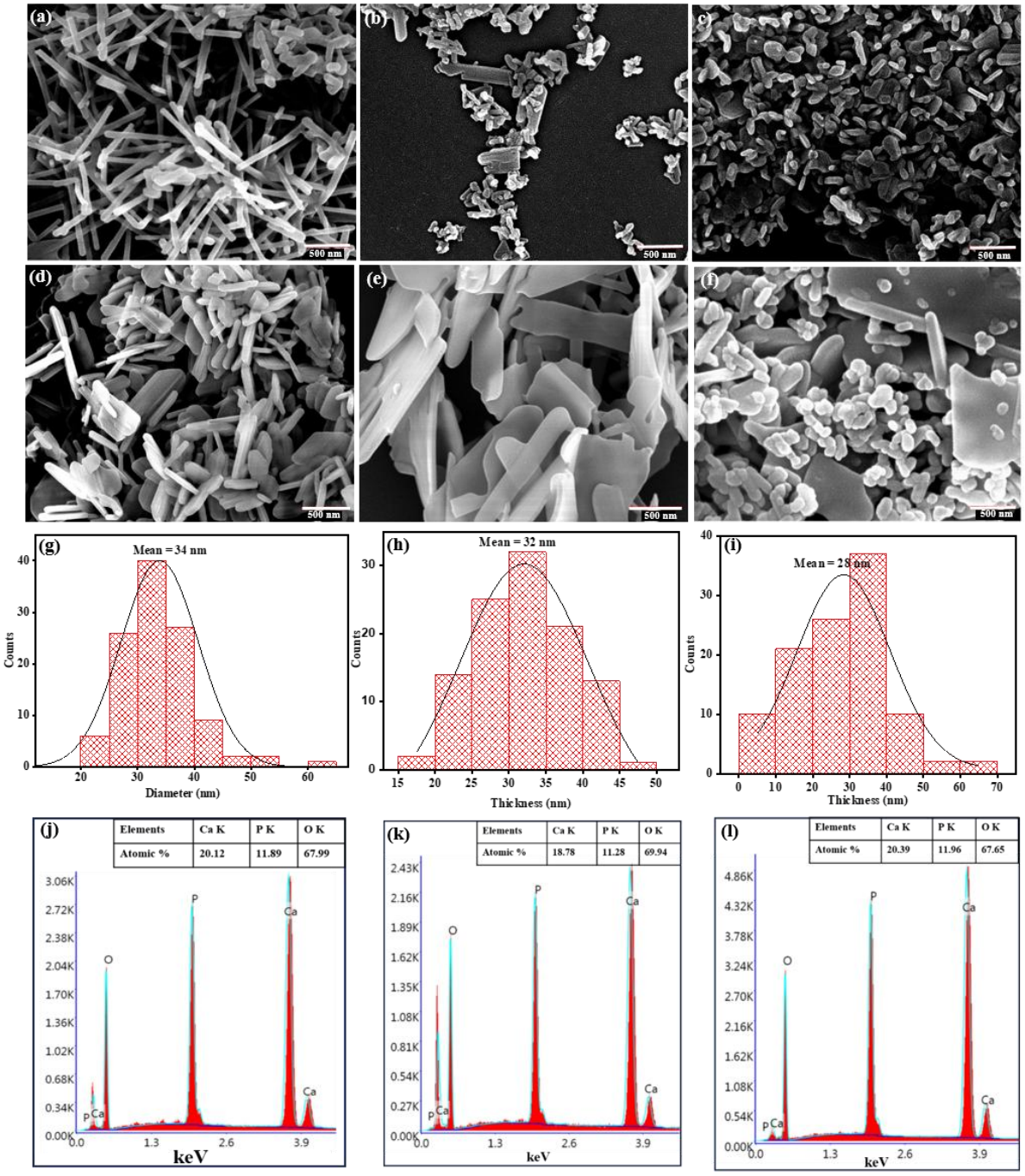

Figure 3.6. Morphological and elemental analyses of as-prepared HA nanocrystals at various pH. *(a – f) FESEM images of as-synthesized HA nanocrystals at various pH* ***:****(a) pH 5 (b) pH 7.5 (c) pH 9 (d) pH 9.5 (e) pH 10 (f) 11. (g – i) The diameter distribution of HA nanorods, synthesized at pH 5 (a), and thickness distribution of HA nanoplates, obtained at pH 9 (b) and 9.5 (c), using histogram plots. (j – l)) The EDX spectra of as-synthesized HA nanorods at pH 5 (a), and HA nanoplates at pH 9 (b) and 9.5 (c).*

The diameter distribution of HA nanorods (HA5) and thickness distribution of HA nanoplates (HA9 and HA9.5) were also demonstrated by histogram plots, for which more than 100 particles were measured from each morphology of HA nanocrystals [Fig. 3.6 (g – i))]. The EDS spectra [Fig. 3.6 (j – l)] confirmed the purity of HA nanocrystals, showing only Ca, P, and O with a Ca/P molar ratio of ~1.67, required for HA formation. The pH-dependent crystal growth mechanism is also discussed using a schematic diagram, as shown in Fig. 3.7.

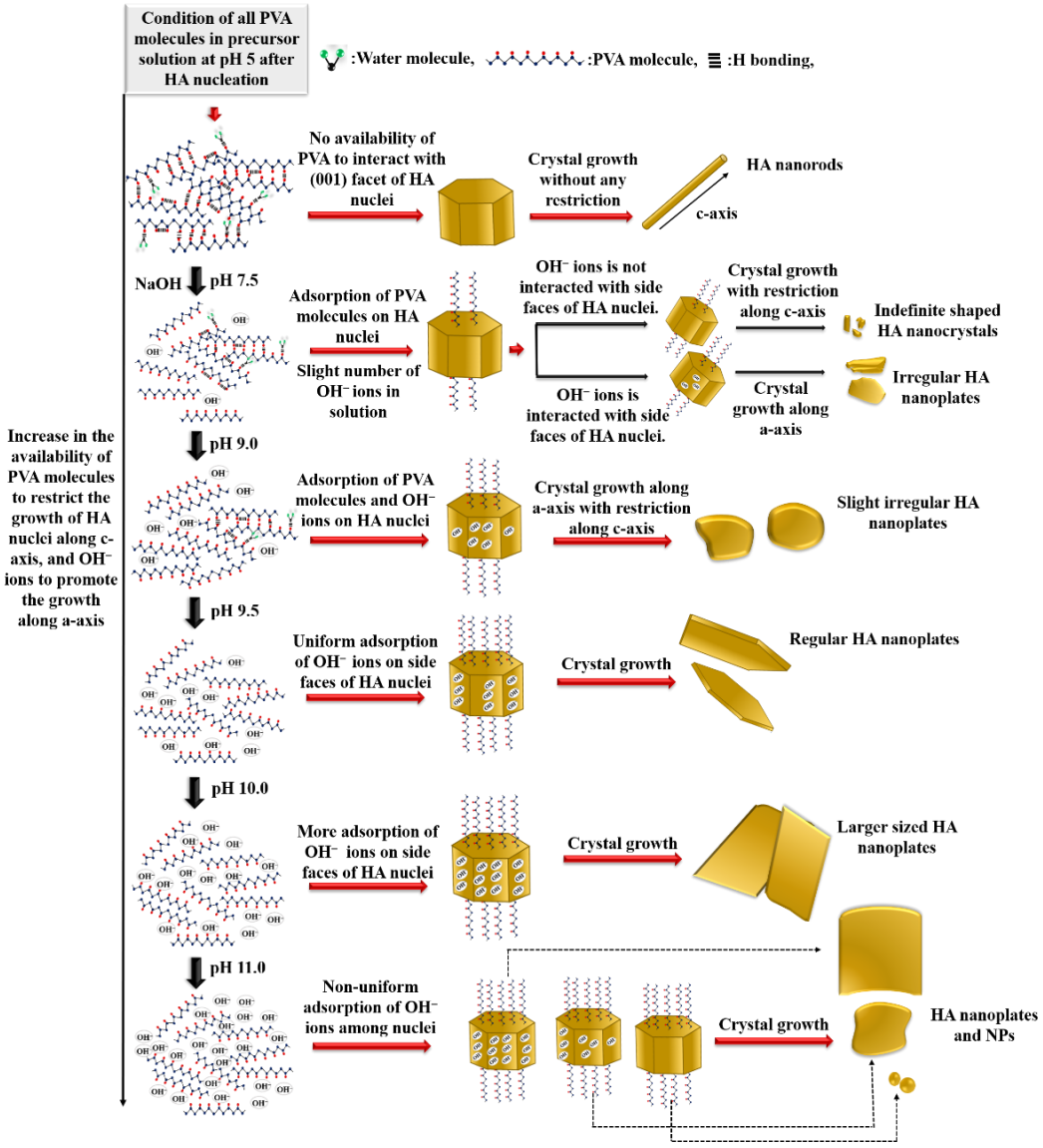

Figure 3.7. *The schematic representation of possible mechanism for the formation of various morphologies of HA nanocrystals at different pH.*

To investigate the effect of HT time on the shape of HA nanoplates, the HT time was varied from 6 to 12 h under the fixed temperature of 200ºC, pH of 9.5 and PVA concentration of 2.13 wt %. The shorter HT treatment produced irregular and thinner (~ 7 – 23 nm) HA nanoplates with lengths micro to nano in scale [Fig. 3.8 A], as the adsorption of PVA molecules on the (001) face only allows a limited number of precursor ions (Ca^{2+}, PO_4^{3-} and OH^-) to reach that face. The HT duration of 12 h provides a longer time to reach more precursor ions on (001) face, producing thicker (up to 40 nm scale) HA nanoplates with length in nanometer scale [Fig. 3.8 B]. According to the Oswalt ripening mechanism, the smaller particles possess higher surface energy and solubility, due to which they dissolve in the reaction medium and reprecipitate onto larger particles to minimize their surface energy [32]. Such rapid crystal growth at 6 h is responsible for the irregular shape and lower crystallinity in thin HA nanoplates [Fig. 3.1 B (i) and 3.8 A]. However, the prolonged HT treatment from 6 to 12 h promotes further dissolution of HA nanoplates due to their lower crystallinity and high pressure inside the sealed autoclave. In this way, HA nanoplates further proceeded through a dissolution-precipitation process, which led to the formation of HA nanoplates with ultra-high crystallinity.

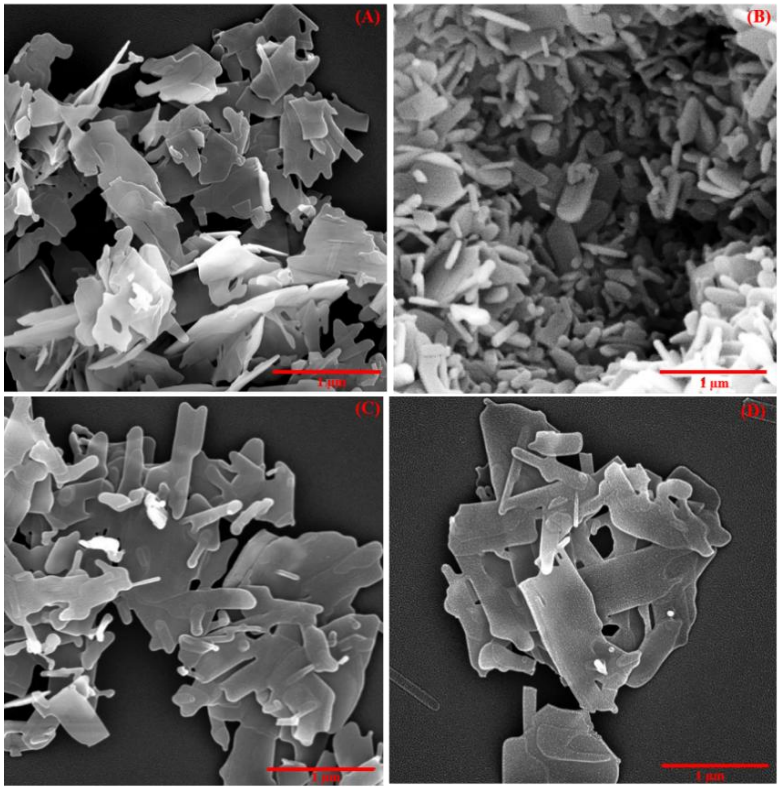

Figure 3.8. Morphology of HA nanocrystals, synthesized under different HT duration and PVA concentrations. *FESEM images of HA nanocrystals, synthesized at HT time of 6 h (A) and 12 h (B) at PVA concentration of 2.13 wt % and pH of 9.5. FESEM images of HA nanocrystals, synthesized under various PVA concentrations of 2.13 wt % (B), 4.17 wt % (C), and 6.13 wt % (D) at pH of 9.5 and HT time of 12 h.*

The increase in the concentration of PVA also significantly affected the thickness of HA nanoplates under HT temperature of 200ºC, time of 12 h, and pH of 9.5. HA nanoplates again transformed to thin nanoplates-like morphology with increasing the PVA concentration from 2.13 to 4.17 wt % [Fig. 3.8 B and C]. This is due to the further increase in the availability of PVA molecules to interact with the (001) face of HA nuclei, which restricts the crystal growth of HA nuclei. Additionally, due to the presence of more PVA molecules in the solution, more NaOH is required to disrupt the hydrogen bonding of PVA molecules with themselves and water molecules. This reduces the number of OH^- ions in the solution, limiting their uniform interaction with the (100) facet of HA nuclei and resulting in irregular thin HA nanoplates. The

thickness and length of such HA thin nanoplates are up to 7 nm and μm in scale, respectively. On further varying the PVA concentration from 4.17 – 6.13 wt. %, no considerable change in the thickness of HA thin nanoplates was observed [Figs. 3.8 C and D]. Higher PVA concentrations in solution require even more NaOH molecules to disturb the hydrogen bonding among themselves and water molecules. However, sufficient NaOH is not available to fully disturb these bonds. Therefore, number of free PVA molecules for the interaction with (001) face of HA nuclei remained same as PVA concentration of 4.17 wt %.

3.5. TEM analyses

TEM, HRTEM and SAED analyses were performed to investigate the morphology, porosity and crystallographic details of HA nanocrystals. Fig. 3.9 A (a1 – c1) shows TEM images of HA5, HA9.5, and HA-6h confirming their rod, plate and thin plate morphologies, respectively, which is consistent with FESEM results. HRTEM images of individual nanoplates [Fig. 3.9 B (b2 – c2)] reveal the porous nature of HA nanoplates, and thin nanoplates with pore diameters in the range of ~ 1.07 – 5.9 nm and ~ 0.6 – 5.2 nm, respectively, where most of them are micropores. This porosity generation on the surface of HA nanoplates (HA9.5) and HA thin nanoplates (HA-6h) is attributed to the removal of PVA molecules from their surface upon calcination [33]. Moreover, the HRTEM images were also recorded to evaluate the crystal growth direction of HA nanocrystals [Fig. 3.9 C (a3 – c3))]. From Fig. 3.9 B (a3), the HA nanorod has a lattice spacing of 0.34 nm related to the (002) plane, indicating crystal growth along the c-axis. In contrast, from Fig. 3.9 C (b3 – c3), the lattice spacing of HA nanoplate and thin nanoplates were calculated to be 0.40 nm and 0.27 nm, which corresponds to (200) and (300) planes, respectively. These results clearly indicate that HA nanoplate and thin nanoplate grew along the a-axis of HA [19, 29, 34, 35]. Further, SAED patterns of HA nanorods (HA5), HA nanoplates (HA9.5) and HA thin nanoplates (HA-6h), as shown in Fig. 3.9 D (a4 – c4), also revealed their single crystalline nature as identified by clear and sharp diffraction spots [8,

19, 36, 37]. The patterns can be easily indexed, according to the space group of *P63/m*, which further confirms the hexagonal phase of HA nanocrystals. The porous nature of HA nanoplates and thin nanoplates were also illustrated in the magnified view [Fig. 3.9 (E)].

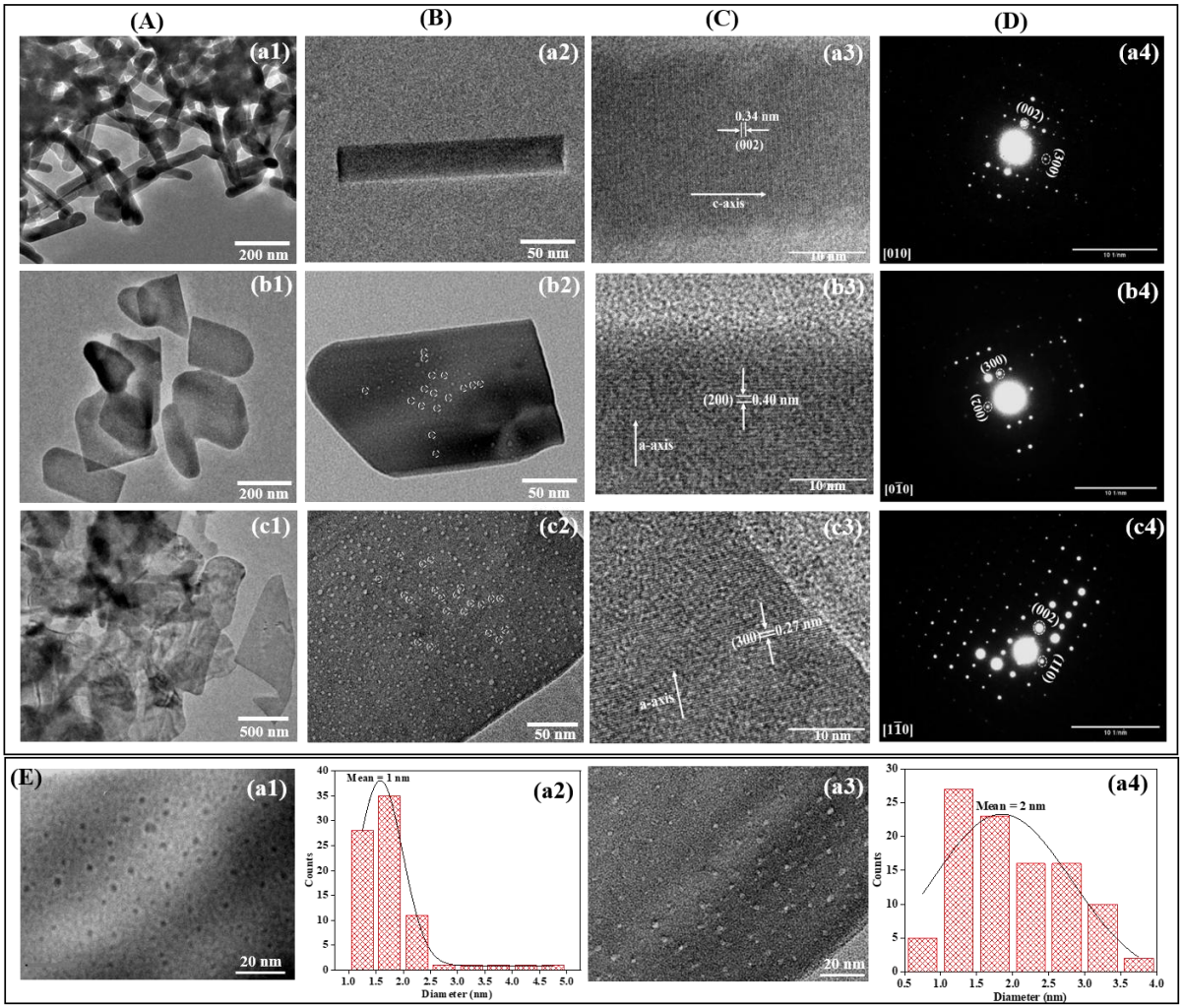

Figure 3.9. Morphological and crystallographic analyses of hydrothermally synthesized HA nanocrystals using TEM. *(A) The Bright field images of HA nanorods (HA5) (a1), HA nanoplates (HA9.5) (b1) and HA thin nanoplates (HA-6h) (c1). (B) The bright field images of single HA nanorods (a2), HA nanoplates (b2) and HA thin nanoplates (c2). (C) The HRTEM images of HA nanorods (a3), HA nanoplates (b3) and HA thin nanoplates (c3), and (D) their corresponding SAED patterns taken along the zone axes [010], [0 $\bar{1}$ 0] and [1 $\bar{1}$ 0] (a4, b4 and c4). (E) The enlarged view of porosity and their distribution (Histogram) on the surface of HA nanoplates (a1 and a2) and HA thin nanoplates (a3 and a4).*

3.6. Summary

This chapter successfully presents the synthesis of bone-like HA nanoplates by hydrothermal method with the use of highly biocompatible and water-soluble PVA as a capping agent. Various experimental parameters, such as pH of solution, PVA concentrations and hydrothermal time were thoroughly optimized to obtain the desired shape of morphology (Fig. 3.10). A regular, flat and well-defined morphology of HA nanoplates with 200 – 500 nm in length, 60 – 250 nm in width, and 7 – 66 nm in thickness, was produced at pH of 9.5, PVA concentration of 2.13 wt %, hydrothermal temperature and time of 200ºC and 12 h, respectively. The developed HA nanoplates were further converted to multiple morphologies, such as HA nanorods and thin nanoplates by tailoring processing parameters. Using HRTEM image, the preferential crystal growth direction was identified along c- and a-axes for HA nanorods, and HA nanoplates and thin nanoplates respectively. Further, the insight mechanisms behind the formation of various morphologies of HA nanocrystals were also discussed in detail. The developed HA nanoplates can be a potential material in the design of bone-mimicking artificial scaffolds for bone tissue engineering application.

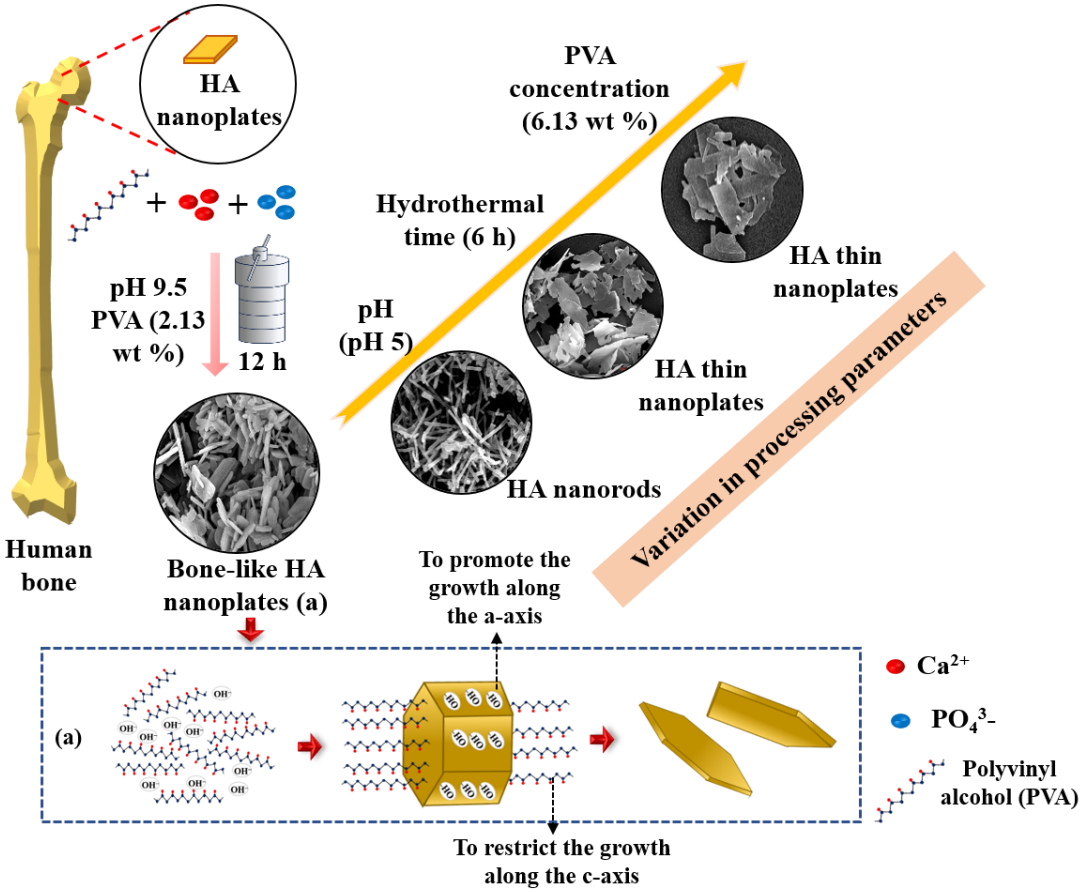

Fig. 3.10 *The schematic diagram, representing the development of bone-like HA nanoplates and their conversion into HA nanorod and thin nanoplate morphologies.*

References

[1] G.A. Martínez-Castañón, J.P. Loyola-Rodríguez, N.V. Zavala-Alonso, S.E. Hernández-Martínez, N. Niño-Martínez, G. Ortega-Zarzosa, F. Ruiz, Preparation and characterization of nanostructured powders of hydroxyapatite, Superficies y vacío 25(2) (2012) 101-105.

[2] H. Kim, R.P. Camata, Y.K. Vohra, W.R. Lacefield, Control of phase composition in hydroxyapatite/tetracalcium phosphate biphasic thin coatings for biomedical applications, Journal of Materials Science: Materials in Medicine 16(10) (2005) 961-966.

[3] W. Liang, Y. Niu, S. Ge, S. Song, J. Su, Z. Luo, Effects of hydrothermal treatment on the properties of nanoapatite crystals, International journal of nanomedicine 7 (2012) 5151-8.

[4] V. Perebeinos, S.-W. Chan, F. Zhang, 'Madelung model' prediction for dependence of lattice parameter on nanocrystal size, Solid State Communications 123(6) (2002) 295-297.

[5] P.M. Diehm, P. Ágoston, K. Albe, Size-Dependent Lattice Expansion in Nanoparticles: Reality or Anomaly?, ChemPhysChem 13(10) (2012) 2443-2454.

[6] M. Ghosh, D. Karmakar, S. Basu, S.N. Jha, D. Bhattacharyya, S.C. Gadkari, S.K. Gupta, Effect of size and aspect ratio on structural parameters and evidence of shape transition in zinc oxide nanostructures, Journal of Physics and Chemistry of Solids 75(4) (2014) 543-549.

[7] Z. Zhu, T. Andelman, M. Yin, T.-L. Chen, S.N. Ehrlich, S.P. O'Brien, R.M. Osgood, Synchrotron x-ray scattering of ZnO nanorods: Periodic ordering and lattice size, Journal of Materials Research 20(4) (2005) 1033-1041.

[8] M. Jevtić, M. Mitrić, S. Škapin, B. Jančar, N. Ignjatović, D. Uskoković, Crystal Structure of Hydroxyapatite Nanorods Synthesized by Sonochemical Homogeneous Precipitation, Crystal Growth & Design 8(7) (2008) 2217-2222.

[9] E. Doustkhah, R. Najafi Zare, Y. Yamauchi, A. Taheri-Kafrani, H. Mohtasham, M. Esmat, Y. Ide, N. Fukata, S. Rostamnia, M.H. Sadeghi, M.H.N. Assadi, Template-oriented synthesis

of hydroxyapatite nanoplates for 3D bone printing, Journal of Materials Chemistry B 7(45) (2019) 7228-7234.

[10] J.S. Cho, S.-H. Rhee, Formation mechanism of nano-sized hydroxyapatite powders through spray pyrolysis of a calcium phosphate solution containing polyethylene glycol, Journal of the European Ceramic Society 33(2) (2013) 233-241.

[11] D. Kong, X. Xiao, X. Qiu, W. Zhang, Y. Yang, Synthesis of Hydroxyapatite Nanorods under Mild Conditions and Their Drug Release Properties, Chinese Journal of Chemistry 33(9) (2015) 1024-1030.

[12] A.J. Nathanael, Y.H. Seo, T.H. Oh, PVP Assisted Synthesis of Hydroxyapatite Nanorods with Tunable Aspect Ratio and Bioactivity, Journal of Nanomaterials 2015 (2015) 621785.

[13] G. Bharath, A. Jagadeesh Kumar, K. Karthick, D. Mangalaraj, C. Viswanathan, N. Ponpandian, Shape evolution and size controlled synthesis of mesoporous hydroxyapatite nanostructures and their morphology dependent Pb(ii) removal from waste water, RSC Advances 4(70) (2014) 37446-37457.

[14] R.R. Kimaka P, P. Wang, M. He, S. Meng, J. Yao, H. Li, C. Yang, Z. Li, Ce- and La-doped polymetallic layered double hydroxides for enhanced oxygen evolution reaction performance at high current density, Science China Chemistry 67(8) (2024) 2586-2598.

[15] H. Esfahani, E. Salahi, A. Tayebifard, M.R. Rahimipour, M. Keyanpour-Rad, Influence of zinc incorporation on microstructure of hydroxyapatite to characterize the effect of pH and calcination temperatures, Journal of Asian Ceramic Societies 2(3) (2014) 248-252.

[16] Y. In, U. Amornkitbamrung, M.-H. Hong, H. Shin, On the Crystallization of Hydroxyapatite under Hydrothermal Conditions: Role of Sebacic Acid as an Additive, ACS Omega 5(42) (2020) 27204-27210.

[17] F. Ren, Y. Ding, Y. Leng, Infrared spectroscopic characterization of carbonated apatite: A combined experimental and computational study, Journal of Biomedical Materials Research Part A 102(2) (2014) 496-505.

[18] E.A. Taylor, C.J. Mileti, S. Ganesan, J.H. Kim, E. Donnelly, Measures of Bone Mineral Carbonate Content and Mineral Maturity/Crystallinity for FT-IR and Raman Spectroscopic Imaging Differentially Relate to Physical–Chemical Properties of Carbonate-Substituted Hydroxyapatite, Calcified Tissue International 109(1) (2021) 77-91.

[19] F. Ren, Y. Ding, X. Ge, X. Lu, K. Wang, Y. Leng, Growth of one-dimensional single-crystalline hydroxyapatite nanorods, Journal of Crystal Growth 349(1) (2012) 75-82.

[20] P. Upadhyay, A. Ullah, Facile synthesis of hydroxyapatite nanoparticles from eggshell biowaste using Azadirachta indica extract as a green template, New Journal of Chemistry 48(3) (2024) 1424-1435.

[21] H. Atta, K.R. Mahmoud, E.S.I. Salim, E. Elmohsnawy, A. El-Shaer, Correlation between positron annihilation lifetime and photoluminescence measurements for calcined Hydroxyapatite, Scientific Reports 14(1) (2024) 10370.

[22] A.A. Bonapasta, F. Buda, P. Colombet, G. Guerrini, Cross-Linking of Poly(Vinyl Alcohol) Chains by Ca Ions in Macro-Defect-Free Cements, Chemistry of Materials 14(3) (2002) 1016-1022.

[23] D. Jahani, A. Nazari, J. Ghourbanpour, A. Ameli, Polyvinyl Alcohol/Calcium Carbonate Nanocomposites as Efficient and Cost-Effective Cationic Dye Adsorbents, Polymers, 2020.

[24] Y. Bao, X. Huang, J. Xu, S. Cui, Effect of Intramolecular Hydrogen Bonds on the Single-Chain Elasticity of Poly(vinyl alcohol): Evidencing the Synergistic Enhancement Effect at the Single-Molecule Level, Macromolecules 54(15) (2021) 7314-7320.

[25] K. Suchanek, A. Bartkowiak, M. Perzanowski, M. Marszałek, From monetite plate to hydroxyapatite nanofibers by monoethanolamine assisted hydrothermal approach, Scientific Reports 8(1) (2018) 15408.

[26] H. Maeda, T. Kawai, S. Sekii, Intra- and intermolecular hydrogen bonds in polyvinyl alcohol solutions, Journal of Polymer Science 35(128) (1959) 288-292.

[27] M.J. Nugent, A. Hanley, P.T. Tomkins, C.L. Higginbotham, Investigation of a novel freeze-thaw process for the production of drug delivery hydrogels, Journal of materials science. Materials in medicine 16(12) (2005) 1149-58.

[28] M.A. Darabi, A. Khosrozadeh, Y. Wang, N. Ashammakhi, H. Alem, A. Erdem, Q. Chang, K. Xu, Y. Liu, G. Luo, A. Khademhosseini, M. Xing, An Alkaline Based Method for Generating Crystalline, Strong, and Shape Memory Polyvinyl Alcohol Biomaterials, Advanced Science 7(21) (2020) 1902740.

[29] C. Zhang, J. Yang, Z. Quan, P. Yang, C. Li, Z. Hou, J. Lin, Hydroxyapatite Nano- and Microcrystals with Multiform Morphologies: Controllable Synthesis and Luminescence Properties, Crystal Growth & Design 9(6) (2009) 2725-2733.

[30] X. Wang, L. Zhang, Z. Liu, Q. Zeng, G. Jiang, M. Yang, Probing the surface structure of hydroxyapatite through its interaction with hydroxyl: a first-principles study, RSC Advances 8(7) (2018) 3716-3722.

[31] D.-J. Wu, Z.-X. Liu, C.-Z. Gao, X.-C. Shen, X.-M. Wang, H. Liang, Effect of methyl and hydroxyl functional group surfaces on crystallization of hydroxyapatite coating, Surface and Coatings Technology 228 (2013) S24-S27.

[32] N. Thanh, N. Maclean, S. Mahiddine, Mechanisms of Nucleation and Growth of Nanoparticles in Solution, Chemical Reviews 114 (2014).

[33] Z. Ecsedi, I. Lazău, C. Păcurariu, Synthesis of mesoporous alumina using polyvinyl alcohol template as porosity control additive, Processing and Application of Ceramics 1 (2007).

[34] G. Zuo, X. Wei, H. Sun, S. Liu, P. Zong, X. Zeng, Y. Shen, Morphology controlled synthesis of nano-hydroxyapatite using polyethylene glycol as a template, Journal of Alloys and Compounds 692 (2017) 693-697.

[35] P. Wang, S. Meng, B. Zhang, M. He, P. Li, C. Yang, G. Li, Z. Li, Sub-1 nm Cu2O Nanosheets for the Electrochemical CO2 Reduction and Valence State–Activity Relationship, Journal of the American Chemical Society 145(48) (2023) 26133-26143.

[36] A.J. Nathanael, S.I. Hong, T.H. Oh, Y.H. Seo, D. Singh, S.S. Han, Enhanced cell viability of hydroxyapatite nanowires by surfactant mediated synthesis and its growth mechanism, RSC Advances 6(30) (2016) 25070-25081.

[37] Y. Wen, J. Liu, F. Zhang, Z. Li, P. Wang, Z. Fang, M. He, J. Chen, W. Song, R. Si, L. Wang, Mesoporous MnO2 nanosheets for efficient electrocatalytic nitrogen reduction via high spin polarization induced by oxygen vacancy, Nano Research 16(4) (2023) 4664-4670.